

Bayesian model selection for testing the no-hair theorem with black hole ringdowns

S. Gossan, J. Veitch, and B. S. Sathyaprakash

School of Physics and Astronomy, Cardiff University, 5, The Parade, Cardiff, UK, CF24 3YB

(Dated: June 5, 2022)

General relativity predicts that a black hole that results from the merger of two compact stars (either black holes or neutron stars) is initially highly deformed but soon settles down to a quiescent state by emitting a superposition of quasi-normal modes (QNMs). The QNMs are damped sinusoids with characteristic frequencies and decay times that depend only on the mass and spin of the black hole and no other parameter – a statement of the no-hair theorem. In this paper we have examined the extent to which QNMs could be used to test the no-hair theorem with future ground- and space-based gravitational-wave detectors. We model departures from general relativity (GR) by introducing extra parameters which change the mode frequencies or decay times from their general relativistic values. With the aid of numerical simulations and Bayesian model selection, we assess the extent to which the presence of such a parameter could be inferred, and its value estimated. We find that it is harder to decipher the departure of decay times from their GR value than it is with the mode frequencies. Einstein Telescope (ET, a third generation ground-based detector) could detect departures of $< 1\%$ in the frequency of the dominant QNM mode of a $500 M_\odot$ black hole, out to a maximum range of 4 Gpc. In contrast, the New Gravitational Observatory (NGO, an ESA space mission to detect gravitational waves) can detect departures of $\sim 0.1\%$ in a $10^8 M_\odot$ black hole to a luminosity distance of 30 Gpc ($z = 3.5$).

PACS numbers:

I. INTRODUCTION

Merging compact binaries consisting of neutron stars or black holes are promising sources [1] of gravitational radiation for advanced gravitational wave detectors that are currently being built [2, 3]. These sources are also potential laboratories for testing general relativity (GR) in the strong field regime [4–8]. The result of such an event (with sufficiently massive progenitors) is a highly perturbed black hole (BH) which rapidly returns to its quiescent state (i.e., a Kerr BH [9]), through the emission of gravitational waves (GWs). The perturbation, and therefore the emitted radiation, can be expanded in the natural basis of oscillations, the quasi-normal modes (QNMs) [10] (for a recent review on QNM see, e.g., [11]). A Kerr black hole is characterised only by its mass and angular momentum, and so are the complex frequencies of its QNM oscillations [12, 13], although the relative amplitudes of the modes depend on the specific details of the excitation.

Detection of the characteristic ringdown GW signal of a BH would, therefore, allow a direct test of the no-hair theorem [14], and hence GR, through the comparison of frequencies and decay times of these modes with the predictions of GR for a BH with certain mass and spin. In practice, the detection and discrimination of multiple modes is essential, as it is first necessary to infer the mass and spin of the black hole before checking for consistency between the modes. If any of the modes have some parameter dependence, other than mass and spin, then the mass and spin obtained from these modes will not be consistent with that obtained from the others, and thus the source of emission must not be a Kerr black hole.

In Ref. [14] Dreyer *et al* first developed the formalism for testing GR with QNM. They also suggested the test

of the no hair theorem through the measurement of more than one mode. Berti *et al*, [15, 16] investigated the accuracy of measurement of individual mode parameters using a Fisher matrix analysis and estimated the resolvability of individual modes in the complete signal as a function of signal-to-noise ratio. Their main conclusion is that mode resolvability is going to be pretty difficult. Kamaretsos *et al* showed recently that using black hole ringdown signals that are emitted after a binary merges, it is possible to recover the mass ratio of the progenitor binary from relative amplitudes of the QNMs [17]. They also proposed different ways of testing GR using QNMs. In particular, they proposed that it is sufficient to use any three of the observed frequencies and decay times for checking the consistency of the ringdown signal with GR. This *minimal set* of parameters makes the test may be far more effective than trying to resolve the different mode frequencies and decay times. This is one approach we shall follow in this work.

More specifically, in this paper we demonstrate the feasibility of the proposal in Ref. [17]. We will show that it is possible to infer the total mass and spin of the black hole and the mass ratio of the progenitor binary from the observed ringdown GW, using a phenomenological mapping from these to the mode parameters. Having established this, we extend our waveform model to include arbitrary deviations from the predicted values of the frequencies and decay times, which can be estimated either along with the physical parameters of the source or on their own, if we assume no relationship between the complex QNM frequencies and the mass and angular momentum of the BH. This gives us two methods of testing GR:

1. Measure the QNM parameters individually and check for consistency between the implied mass and

angular momentum from each of the modes.

2. Assume that the GR waveform is broadly correct but allow deviations in the parameters of a subset of the QNMs away from their predicted values and then perform model selection between the GR and non-GR models.

We study both of these techniques in the context of future space- and ground-based detectors, particularly the Einstein Telescope [18, 19] and a rescoped version of the Laser Interferometer Space Antenna called New Gravitational Observatory (NGO).

The paper is organised as follows: Section II defines the waveform model and analysis methods used, Section III describes the simulations of ground- and space-based observations, and Section IV contains comparisons of the two methods used here in testing GR and conclusions.

II. ANALYSIS

In this Section we will discuss the nature of the ringdown waveform used in this study. The main focus will be to use a superposition of quasi-normal modes containing not only the dominant mode but also the first two sub-dominant ones. Ringdown signals that we study are assumed to be emitted by deformed black holes that form from the merger of compact binaries consisting of *non-spinning* components. The latter assumption allows us to use a phenomenological waveform model based on numerical relativity simulations; the observed signal is characterised by only three intrinsic parameters: the mass and spin of the final black hole and the mass ratio of the progenitor binary.

A. Ringdown model

A perturbed black hole emits a spectrum of modes characterized by three numbers (l, m, n) . Indices $l = 2, 3, \dots$, and $m = -l, \dots, +l$, are the well-known spherical harmonic indices, and $n = 0, 1, 2, \dots$, is the mode overtone index. Overtones other than the fundamental $n = 0$ mode are not excited with significant amplitudes. We shall therefore only consider the fundamental mode and drop the index from further discussion.

The two polarisations of the gravitational waveform, h_+ and h_\times , emitted by a BH of mass M during its ringdown are described as the sum over the QNMs,

$$h_+ = \frac{M}{r} \sum_{l,m>0} A_{l|m|} e^{-t/\tau_{lm}} Y_+^{lm} \cos(\omega_{lm}t + \varphi_{lm} - m\phi), \quad (1)$$

$$h_\times = \frac{M}{r} \sum_{l,m>0} A_{l|m|} e^{-t/\tau_{lm}} Y_\times^{lm} \sin(\omega_{lm}t + \varphi_{lm} - m\phi). \quad (2)$$

Here r is the luminosity distance to black hole, $A_{l|m|}(q)$ are the mode amplitudes that depend only on the ratio $q = m_1/m_2$ ($m_1 > m_2$) of the component masses of the progenitor binary, and $\tau_{lm}(M, j)$ and $\omega_{lm}(M, j)$ are the characteristic mode damping times and frequencies. The mode damping times and frequencies depend only the black hole mass M and its spin j , but they are difficult to compute analytically. It is necessary to use numerical methods to compute them [11]. Fits to some of the lower order modes can be found in Berti et al [15]. φ_{lm} are the constant phases of the modes at the epoch of observation $t = 0$ from the observer's location. In this work we assume all $\varphi_{lm} = 0$ for our simulations and parameter estimation. $\iota \in [0, \pi)$ is the angle between the BH spin-axis and the line-of-sight to the observer and $\phi \in [0, 2\pi]$ is the azimuth angle of the black hole with respect to the observer. $Y_{+,\times}^{lm}(\iota)$ are the sum of spin -2 weighted spherical harmonics,

$$Y_+^{lm}(\iota) \equiv -2Y^{lm}(\iota, 0) + (-1)^l -2Y^{l-m}(\iota, 0), \quad (3)$$

$$Y_\times^{lm}(\iota) \equiv -2Y^{lm}(\iota, 0) - (-1)^l -2Y^{l-m}(\iota, 0). \quad (4)$$

Although the waveform in Eqs. (1) and (2) contains a summation of modes over all values of l and m , the relative amplitudes of the higher order modes are significantly less than those of the lower, so we restrict the sum to the most significant modes. The waveform considered for this analysis is a superposition of the $n = 0$, $l = 2$, $m = 1$ and $n = 0$, $l = m = \{2, 3, 4\}$ modes (which will hereafter be referred to as the 21, 22, 33 and 44 modes, respectively) with the 22 mode being dominant.

The relative dominance of the higher order modes is dependent on the specific excitation that occurred (through A_{lm}) and the position of the observer (through Y_{lm}). This depends on both the mass ratio $q = m_1/m_2 \geq 1$ of the compact binary components prior to merger, and ι . We used a phenomenological model based on fits to a set of numerical simulations to describe the mode amplitudes, as in Kamaretsos *et al* [17]. For simplicity, all amplitudes, except that of the 22 mode, are expressed relative to the 22 mode,

$$A_{22} = 0.25 \exp\left(-\frac{q}{7.5}\right) \quad (5)$$

$$\frac{A_{33}}{A_{22}} = 0.182 (q - 1)^{0.321} \quad (6)$$

$$\frac{A_{44}}{A_{22}} = 0.0239 q^{0.77} \quad (7)$$

$$\frac{A_{21}}{A_{22}} = 0.133 (q - 1)^{0.486} \quad (8)$$

Instead of damping times τ_{lm} it is customary to use *quality factors* Q_{lm} defined by $Q_{lm} = 2\omega_{lm}\tau_{lm}$. Berti et al [15] provide a simple fitting formula to all mode frequencies and quality factors they considered which is of the form:

$$M\omega = f_1 + f_2(1 - j)^{f_3} \quad (9)$$

$$Q = q_1 + q_2(1 - j)^{f_3} \quad (10)$$

where f_1, f_2, f_3, q_1, q_2 and q_3 are fitting constants. For the modes considered in this paper Table I lists the fitting constants.

(l, m)	f_1	f_2	f_3	q_1	q_2	q_3
(2, 1)	0.6000	-0.2339	0.4175	-0.3000	2.3561	-0.2277
(2, 2)	1.5251	-1.1568	0.1292	0.7000	1.4187	-0.4990
(3, 3)	1.8956	-1.3043	0.1818	0.9000	2.3430	-0.4810
(4, 4)	2.3000	-1.5056	0.2244	1.1929	3.1191	-0.4825

TABLE I: The fitting constants in Eqns. (9) and (10), for the 21, 22, 33 and 44 modes [15].

The gravitational-wave strain observed by a detector due to the excitation of QNM can be expressed as

$$h = F_+ h_+ + F_\times h_\times \quad (11)$$

where F_+ and F_\times are the detector antenna pattern functions, which depend on the position (θ, φ) of the black hole relative to the detector and polarisation angle ψ of the radiation (see Ref. [17] for details).

B. A generalised model for the QNM

In order to test GR, we extended the waveform model so that the frequencies and decay times of the modes were allowed to be dependent not only on M and j , but also other dimensionless parameters. More specifically, we considered that frequencies ω_{lm} depended on three parameters $(M, j, \Delta\hat{\omega}_{lm})$ and damping times τ_{lm} also depended on three parameters $(M, j, \Delta\hat{\tau}_{lm})$. Furthermore, we assumed that the dimensionless parameters $\Delta\hat{\omega}_{lm}$ and $\Delta\hat{\tau}_{lm}$ were independent for each mode. Following Li et al [20], in this generalised model, the frequencies $\omega_{lm, \text{nonGR}}$ and decay times $\tau_{lm, \text{nonGR}}$ were expressed as

$$\omega_{lm, \text{nonGR}} = \omega_{lm, \text{GR}} (1 + \Delta\hat{\omega}_{lm}) \quad (12)$$

$$\tau_{lm, \text{nonGR}} = \tau_{lm, \text{GR}} (1 + \Delta\hat{\tau}_{lm}) \quad (13)$$

where $\omega_{lm, \text{GR}}$ and $\tau_{lm, \text{GR}}$ are the frequencies and decay times of modes as in GR. The signal produced by the GR hypothesis is a special case of the generalised model, in which $\Delta\hat{\omega}_{lm} = \Delta\hat{\tau}_{lm} = 0$ for all l, m .

C. Bayesian analysis

Having described the waveform model and its parameters (contained in a parameter vector $\vec{\theta}$), we will now describe how these parameters are estimated from data containing a ringdown signal. We assume that the data from the gravitational wave detector in the frequency domain \tilde{d} contains both the ringdown signal $\tilde{h}(f; \vec{\theta})$ and some additive Gaussian noise with known power spectrum $S_h(f)$. Thus, the data \tilde{d} is assumed to be $\tilde{d}_i = \tilde{h}(f_i; \vec{\theta}) + \tilde{n}_i$, where i is the index of the frequency bin. The noise

power spectra used for ET and NGO are given in Section III A. As we perform our analysis in the frequency domain, we use the Fourier transformed signal model $\tilde{h}(f) = \int_0^\infty h(t) e^{-2\pi i f t} dt$ computed with the FFTW package.

Our goal is to compute the posterior probability distribution (PDF) (see, for instance, f[21]), or the parameters $p(\vec{\theta}|d, \mathcal{H})$,

$$p(\vec{\theta}|d, \mathcal{H}) = \frac{p(d|\vec{\theta}, \mathcal{H})p(\vec{\theta}|\mathcal{H})}{p(d|\mathcal{H})}, \quad (14)$$

where $p(d|\mathcal{H}) = \int_{\Theta} p(\vec{\theta}|\mathcal{H})p(d|\vec{\theta}, \mathcal{H})d\vec{\theta}$ is the evidence, or marginal likelihood, of the model \mathcal{H} , $p(\vec{\theta}|\mathcal{H})$ is the prior distribution and

$$p(d|\vec{\theta}, \mathcal{H}) \propto \exp \left(-2 \int_0^\infty \frac{|d - h(f; \vec{\theta})|^2}{S_h(f)} df \right) \quad (15)$$

is the likelihood of the data for a particular set of parameters $\vec{\theta}$. Posterior distributions for particular parameters of interest, e.g. the $\Delta\hat{\omega}_{lm}$ and $\Delta\hat{\tau}_{lm}$, are computed by marginalising the PDF over all other parameters. We also compute the Bayes factor $B_{i,j}$ between various hypotheses, $B_{i,j} = p(d|i)/p(d|j)$, which is the evidence ratio between hypotheses i and j . Due to the large range of this quantity we will always use the natural logarithm of this, $\log B_{i,j}$, in section III D.

To compute the PDFs and evidence we use the `inspnest` implementation of the nested sampling algorithm, described in [21], modified to use the ringdown signal model, which is available as part of the LSC Algorithm Library [22]. The end product of the analysis is the model evidence and a set of samples from the posterior PDF that are histogrammed to produce the figures below.

III. SIMULATIONS

A. Sensitivity curves

In this paper, the ET and NGO detectors are considered. For simulations concerning ET, the power spectral density corresponding to the ET-B sensitivity curve is considered, described by $S_h(f) = 10^{-50} h_n(f)^2 \text{ Hz}^{-1}$, where $h_n(f)$ is given by

$$h_n(f) = 2.39 \times 10^{-27} x^{-15.64} + 0.349 x^{-2.145} + 1.76 x^{-0.12} + 0.409 x^{1.10}$$

and $x = f/100 \text{ Hz}$. For NGO, the sensitivity curve associated with the $L = 1 \times 10^9 \text{ m}$ arm, 4-link mission studied in [23], which corresponds to a power spectral density given by

$$S_h(f) = \frac{10}{3L^2} \left(1 + \left[\frac{2Lf}{0.41c} \right]^2 \right) (4S_{acc} + S_0) \quad (16)$$

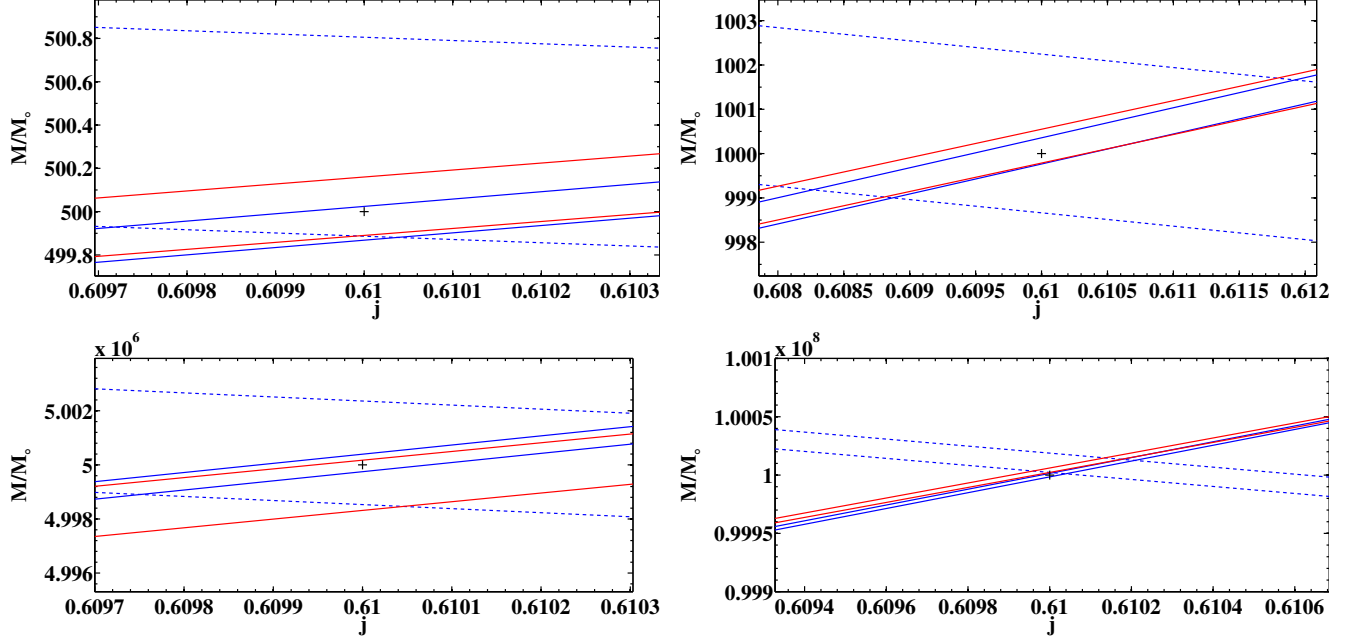


FIG. 1: Projections in the (M, j) -plane of the 90% confidence limits on ω_{22} , τ_{22} and ω_{33} (blue, blue dotted and red lines respectively) for injections of $M = 500 M_\odot$ (top-left at 125 Mpc; SNR = 4198), $M = 1000 M_\odot$, (top-right at 225 Mpc; SNR = 3596); $M = 5 \times 10^6 M_\odot$ (bottom-left at 1 Gpc; SNR = 8010) and $M = 10^8 M_\odot$ (bottom-right at 1 Gpc; SNR = 123165). The injected value is denoted in each case by a crosshair.

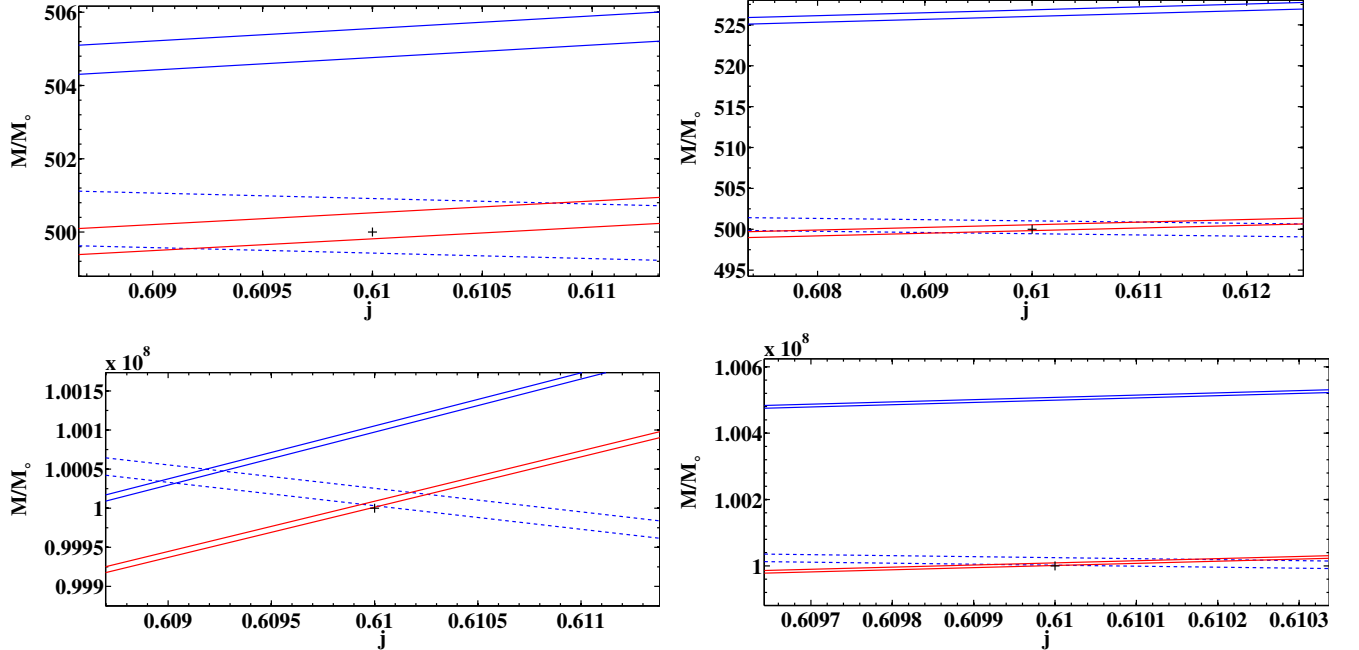


FIG. 2: Projections in the (M, j) -plane of the 90% confidence limits on ω_{22} , τ_{22} and ω_{33} (blue, blue dotted and red lines respectively) for injections of $M = 500 M_\odot$ (top at 125 Mpc; SNR = 4179 (left) and 4062 (right)) and $10^8 M_\odot$ (bottom at 1 Gpc; SNR = 123137 (left) and 123023 (right)) with $\Delta\hat{\omega}_{22} = -0.001$ and -0.005 (left and right columns respectively). The injected value is denoted in each case by a crosshair.

where, $S_0 = 1.153 \times 10^{-22} \text{ m}^2 \text{ Hz}^{-1}$ and

$$S_{acc} = 1.37 \times 10^{-32} \left(1 + \frac{10^{-4} \text{ Hz}}{f} \right) \left(\frac{2\pi f}{1 \text{ Hz}} \right)^{-4} \text{ m}^2 \text{ Hz}^{-1} \quad (17)$$

B. Choice of injection parameters

The GW signal emitted from the QNM of a black hole ringdown as observed in a detector network depends on the mass and spin of the final BH, the mass ratio of the progenitor binary and other extrinsic parameters that describe the orientation of the black hole, its distance from the detector and its position on the sky. For the different sensitivity bands of ET and NGO we chose the following range of source parameters to ensure a detectable signal in each case.

For ET, black holes of observed mass $500 M_\odot$ and $1000 M_\odot$ at luminosity distances, D_L , from 125 Mpc and 225 Mpc respectively, out to 6.63 Gpc (corresponding to redshift $z \simeq 1$ [24]) were considered. For NGO, black holes of observed mass 5×10^6 and $10^8 M_\odot$ at $D_L = 1 - 58.9$ Gpc (with the upper limit corresponding to redshift $z \simeq 6$) were considered. In both cases, the source position (α, δ) was set to be directly above the detector at the time of observation (ensuring the greatest amplitude response to the incoming signal). For all systems, the inclination and polarisation angles (ι, ϕ) were set to $(\frac{\pi}{3}, \frac{\pi}{3})$, and the initial phase of the different modes were assumed to be zero. The mass ratio q of the binary system prior to merger and the spin j of the black hole after merger were set to $q = 2$ and $j = 0.61$, respectively. For the sake of using the phenomenological fit in table I the binary components were assumed to be non-spinning. It is important to note, especially for NGO, that the observed mass of the system is redshifted to be greater than the intrinsic mass of the system by a factor of $(1+z)$. Here we report this observed, redshifted mass for injections and recovery.

For GR injections, parameters $\Delta\hat{\omega}_{lm} = \Delta\hat{\tau}_{lm} = 0$, whereas for non-GR injections, either $\Delta\hat{\omega}_{22}$ or $\Delta\hat{\tau}_{22}$ was varied in the range $-0.01 \dots -0.1$, with all other $\Delta\hat{\omega}_{lm} = \Delta\hat{\tau}_{lm} = 0$.

C. Constraining QNM parameters

Having established the parameters of our test sources, we now move on to consider the two tests of GR. The first method broadly follows the outline of [17] to estimate the parameters of each QNM in the ringdown signal. By choosing two of the measurements one can infer the true mass and spin of the black hole by excluding regions in the M, j plane which are inconsistent with the measured parameters. The third measurement is then used to confirm the consistency of the inference. In the case of GR the allowed area will intersect both the previous areas as

in Figure 1. Alternatively, if the signal is inconsistent with GR the intersections of the confidence regions will not agree, as in Figure 2.

In order to compute the constraints, we find the upper and lower 90% probability interval of the marginal posterior probability distribution of the parameters $\Delta\hat{\omega}_{lm}$ and $\Delta\hat{\tau}_{lm}$. In each case the injected values of these parameters were set to 0, corresponding to the GR waveform. The priors for $\Delta\hat{\tau}_{lm}$ and $\Delta\hat{\omega}_{lm}$ were all uniform in the interval $[-1.0, 0.3]$ for all analyses, and the M, j and q parameters were set to their injected values. As we are estimating the mode parameters directly, through $\Delta\hat{\omega}_{lm}$ and $\Delta\hat{\tau}_{lm}$, the values of M and j parameters do not play any role in the results other than to set the centre of the prior range. The reason for the asymmetric choice of interval is that by allowing $\Delta\hat{\omega}_{22}$ to be greater than 0.3, the frequencies of the 22 and 33 modes collide, leading to strong correlations between the parameters of these modes upon recovery and confusion between the modes. Note that we allow the frequency of the 33 mode to vary downward into the band of the 22 mode, but this does not result in difficulties as the 22 mode is already within this band, making identification easier. In all searches, the luminosity distance of the source and orientation angles are assumed known and fixed to the aforementioned values.

We chose the $\Delta\hat{\omega}_{22}$, $\Delta\hat{\tau}_{22}$ and $\Delta\hat{\omega}_{33}$ parameters to perform our consistency test as these are the three recovered with the greatest precision for the signals we considered, and will therefore give the most stringent test.

We first injected signals using the GR waveform and performed parameter estimation on the three test parameters. The 90% probability limits on ω_{lm} and τ_{lm} were projected in the (M, j) -plane to show visually the consistency test between the three modes, and that they agree at the injected value (M, j) within the measurement accuracy. Figure 1 shows that for each system, the projections of ω_{lm} and τ_{lm} coincide at the same position, and the region of coincidence encloses the injected value of the mass and spin of the system, as expected.

To contrast, in Figure 2 we show the corresponding plots where the injection is performed with deviations from GR of $\Delta\hat{\omega}_{22}$ of -0.01 and -0.05 for ET, whilst for NGO deviations of -0.001 and -0.005 were considered (all other parameters are the same).

This demonstrates the feasibility of the method of for testing the no hair theorem using consistency of the modes, when the signal is strong and the modes are clearly distinguishable. Of course, we may not be fortunate enough to observe BH ringdowns from such nearby sources, in which case we expect the power of the method to diminish.

To investigate the accuracy to which the mode parameters are resolvable we performed a set of injections at luminosity distances spanning the entire distance range quoted in Section III B, and estimated the $\Delta\hat{\omega}_{22}$, $\Delta\hat{\omega}_{33}$ and $\Delta\hat{\tau}_{22}$ parameters. For each black hole system considered, the width of the 90% confidence intervals for the

extracted values of $\Delta\hat{\omega}_{lm}$ and $\Delta\hat{\tau}_{lm}$ were plotted against luminosity distance in Figure 3, for injections with GR waveforms. From this figure, it can be seen that the width of the 90% confidence intervals for the values of $\Delta\hat{\omega}_{22,33}$ and $\Delta\hat{\tau}_{22}$ increases with distance, as expected. $\Delta\hat{\omega}_{33}$ is extracted with considerably less accuracy than $\Delta\hat{\omega}_{22}$, because for a black hole system with $q = 2$, as considered here, the 33 mode is significantly less excited than the dominant 22 mode, and thus the 33 mode has a much lower SNR, resulting in poorer resolution. By the same token, $\Delta\hat{\tau}_{22}$ is extracted with considerably less accuracy than both $\Delta\hat{\omega}_{22,33}$, as there is less extractable information from the mode decay times as opposed to the mode frequencies. In general, however, the relative weights and SNRs of each mode depends on the source parameters including orientation, and the noise curve of the detector.

We also see that ET can resolve $\Delta\hat{\omega}_{22}$ with errors of less than 1% at $D_L = 4$ Gpc for the systems considered, in addition to resolving $\Delta\hat{\omega}_{22,33}$ and $\Delta\hat{\tau}_{22}$ with errors of 1.5%, 2.5% and 10% for a black hole of $500 M_\odot$ at $D_L = 6.63$ Gpc.

Further to this, NGO can resolve $\Delta\hat{\omega}_{22}$ to $\sim 0.5\%$ accuracy at $D_L = 58.9$ Gpc ($z = 6$) for both $5 \times 10^6 M_\odot$ and $10^8 M_\odot$ systems, showing good results across the range of masses detectable. The damping times $\Delta\hat{\tau}_{22}$ ($\Delta\hat{\omega}_{33}$) can be resolved to $\sim 4\%$ (2%) and $\sim 1\%$ (0.2%) accuracy for $5 \times 10^6 M_\odot$ and $10^8 M_\odot$ systems, respectively, at this distance, reflecting the poorer resolution of these parameters.

The method outlined above to test the accuracy with which the parameter estimation code can extract the three QNM parameters was applied to the case of non-GR signals ($\Delta\hat{\omega}_{lm}$ or $\Delta\hat{\tau}_{lm}$ set to some value within the range quoted in Section III B, with all other $\Delta\hat{\omega}_{lm} = \Delta\hat{\tau}_{lm} = 0$) from systems of $M = 500 M_\odot$ and $10^8 M_\odot$ in ET and NGO. The QNM corresponding to these systems lie closest to the most sensitive frequency regions of the corresponding detectors, so this test is an optimistic case. Also, the distances used were from the lower end of the range quoted in Section III B. For each non-GR injection, the 90% probability limits on the values of $\Delta\hat{\omega}_{22}$, $\Delta\hat{\omega}_{33}$ and $\Delta\hat{\tau}_{22}$ were extracted and used to project the corresponding confidence limits on ω_{lm} and τ_{lm} in the (M, j) -plane.

Figure 2 shows that even for deviations from GR of as small as 1% (corresponding to $\Delta\hat{\omega}_{22} = -0.01$), the projection of ω_{22} does not intersect consistently with the projections of τ_{22} and ω_{33} , which were unchanged from their GR predicted values. When an additional parameter dependence is introduced for one mode parameter, the mass and spin derived from this modified parameter will not be consistent with the mass and spin derived from the other unchanged parameters. For a deviation of 0.5% for ET and 0.05% for NGO, the projection of ω_{22} does not even touch the projections of τ_{22} and ω_{33} , let alone intersect at the correct value. This shows that in extracting the individual mode parameters from a QNM

signal and projecting them in the (M, j) -plane, it is possible to determine if one, or many, of the mode parameters are not consistent with GR and have some parameter dependence other than on the mass and spin.

D. Discriminating between models

Although we have demonstrated the possibility of performing a consistency test between the QNM parameters by plotting them on the (M, j) plane, this method does not provide a quantitative measure of the consistency as such. In this section we seek to provide such a quantification by performing model selection on two competing models: the standard GR model in which we estimate M , j and q ; and the extended model where we estimate M , j and q but allow the individual mode parameters to vary away from their GR predicted values through the $\Delta\hat{\omega}_{lm}$ and $\Delta\hat{\tau}_{lm}$ parameters. We shall see that even in the event where a source is too distant to allow the consistency method discussed in the previous section to be applied, it could still be possible to perform model selection to distinguish between GR and non-GR models.

Bayesian model selection is a method of determining, for a given signal, whether the GR or non-GR model is more likely by comparing the evidences for each. Note that unlike in the previous case where we estimated the QNM parameters directly, here we are estimating the physical parameters of the source along with deviations from the QNM parameters, where all QNM parameters are allowed to vary together. The reason for this difference is that in estimating the QNM parameters directly we would not have a corresponding GR model with any free parameters unless we also searched over M , j and q . Because in the non-GR case we are measuring five parameters, including the best-determined ones, the resulting joint probability distributions are strongly correlated, although the presence of the 21 mode and the assumption that $\Delta\tau_{33} = 0$ help to break the degeneracy.

Here we compare evidences for both GR and non-GR signals injected into simulated ET and NGO data as described above, but calculate the evidence for each model using the nested sampling algorithm. The ratio of these evidences, known as the Bayes factor, quantifies the support for one model over the other provided by the data. Full computation of the Bayesian evidence automatically takes into account the difference in dimensionality of the parameter space, which penalises the more complex non-GR model accordingly, as we shall see.

Figure 4 displays how the Bayes factor between the GR and non-GR models changes as the deviation of the injected signal from GR increases. For the ET signal, we used a mass of $500 M_\odot$ at a distance of 125 Mpc, giving a signal to noise ratio between 3 928 and 4 198. The NGO simulation used a $10^8 M_\odot$ system at a distance of 1 Gpc, with signal to noise ratio between 122 881 and 123 165. For ET, we varied both $\Delta\hat{\omega}_{22}$ and $\Delta\hat{\tau}_{22}$ in the range -0.1 to 0, whereas for NGO we varied both $\Delta\hat{\omega}_{22}$ and $\Delta\hat{\tau}_{22}$

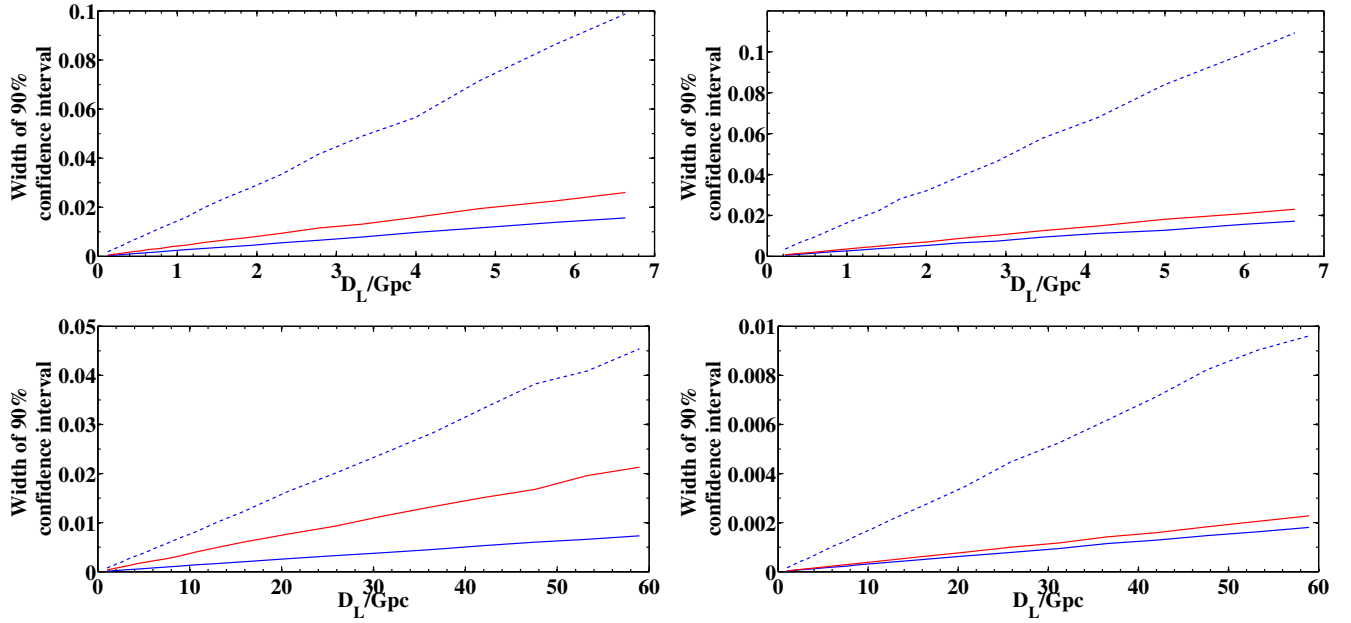


FIG. 3: Width of the 90% confidence intervals for $\Delta\hat{\omega}_{22}$, $\Delta\hat{\omega}_{33}$ and $\Delta\hat{\tau}_{22}$ (blue, red and blue dotted lines respectively) against luminosity distance for injections of 500 (top-left), 1000 (top-right), 5×10^6 (bottom-left) and $10^8 M_\odot$ (bottom-right) for ET (top) and NGO (bottom) simulations.

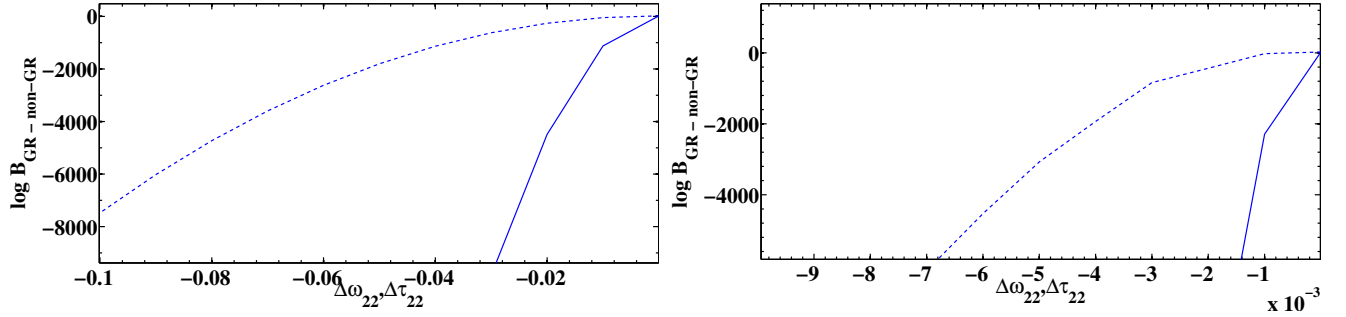


FIG. 4: The differences in evidence between the GR and non-GR models against $\Delta\hat{\omega}_{22}$ and $\Delta\hat{\tau}_{22}$ (blue and blue dotted lines respectively). (Left) For injections of $M = 500$ at 125 Mpc in ET, with SNR between 3928 and 4198. (Right) For injections of $10^8 M_\odot$ in NGO at 1 Gpc, with SNR between 123881 and 123165.

in the range -0.01 to 0 , and in each case computed the evidence for both GR and non-GR models. As the deviation from GR increases, the evidence for the non-GR model increases whilst the evidence for the GR model decreases, causing the Bayes factor (the ratio of evidences for the two models in log space) to increasingly favour the non-GR model, as expected. This is because as the deviation from GR increases, the data fits the GR model with less accuracy, but the parameter freedom of the non-GR model permits a consistency with the data. If we assume a threshold of $\log B_{GR, non-GR} = -10$ (corresponding to prior odds of e^{10} in favour of the non-GR model), below which a deviation is considered significant, then with the source parameters above we are able to distinguish deviations at the level of 1% with ET and NGO for the most sensitive $\Delta\hat{\omega}_{22}$ parameter.

As with the mode resolution of testing GR, the power

of the model selection test decreases with increasing source luminosity distance since the signal visibility decreases. The model selection method was carried out for the sources above at distances spanning the entire range outlined in Section III B, and the Bayes factor between the GR and non-GR minimal set plotted as a function of distance for signals with different deviations from GR. Figure 5 shows that for signals with larger deviations from GR, the maximal set non-GR model is favoured out to much greater distances. We see also that for GR injections, the GR model is indeed preferred, since the simpler model fits the data adequately. When the distance is increased, the size of this effect decreases as the posterior distribution for the modified parameters gradually expands to fill the prior range. The power of the model selection method relies on the ability to exclude parts of the parameter space of the more complex model.

For the purposes of comparison, if we again impose a threshold on the Bayes factor of $\log B_{GR,non-GR} = -10$, we see that the non-GR model is favoured above the threshold at all distances for NGO at a deviation of only 1%, whereas deviations as small as 0.1% can be detected out to a distance of ~ 7.4 Gpc. For ET, we are able to cross the threshold up to ~ 1.61 Gpc for a 2% deviation and 6.63 Gpc for an 8% deviation.

IV. CONCLUSIONS

In this paper we have investigated how well quasi-normal modes could be used to test general relativity. We have confirmed (cf. Section III C) the possibility of constraining deviations from general relativity by measuring the quasi-normal modes of a perturbed black hole with future gravitational-wave detectors. As expected, the $l = 2$, $m = 2$ mode of the signal is the most clearly measurable for the sources we considered, which can be used to infer the mass and spin of the black hole. Measurement of a third parameter, i.e. the frequency of the $l = 3$, $m = 3$ mode, is then used to confirm consistency between the modes. If the true signal is consistent with GR then the measurement of the different parameters would be consistent with one another. Even a 1% deviation was clearly inconsistent for a $500 M_\odot$ source at 125 Mpc in ET and a $10^8 M_\odot$ source at 1 Gpc in NGO.

In Section III D we applied Bayesian model selection to obtain a quantitative measure of the consistency of the data with GR vs a generalised theory where the mode

parameters are allowed to vary. Using this technique, we are able to measure deviations at the 2% level in the $\hat{\omega}_{22}$ parameter out to ~ 1.61 Gpc for a $500 M_\odot$ source with the Einstein Telescope, or deviations at the 0.2% level at $z \sim 2$ with a $10^8 M_\odot$ source with the NGO.

In the above analysis, we have assumed that the location and orientation of the GW source is known prior to the analysis—a significantly simplified analysis compared to the full problem of determining these parameters alongside the test of relativity. Nevertheless, the methods we have developed in this work are equally applicable to the more general case, which should be performed as part of a follow-up study. Moreover, the study has used a very simple model for the ringdown signal that neglects the effect of initially spinning bodies of the progenitor binary. However, our analysis gives optimism that both ET and NGO could be very powerful in testing general relativity and even tiny departures from GR at the level of a percent could be detected. This provides impetus for further investigation of this problem.

V. ACKNOWLEDGEMENTS

The authors gratefully acknowledge support from the Science and Technology Facilities Council (STFC) UK, grant ST/H002006/1. We would like to thank Ioannis Kamaretsos for his input and advice on the simulations, Ilya Mandel for helpful comments, and the LIGO Data-Grid clusters which allowed us to run the simulations used in this paper.

-
- [1] J. Abadie et al. (LIGO Scientific Collaboration) (2010), arXiv:1003.2480.
 - [2] B. Abbott et al., Tech. Rep. LIGO-M060056-08-M, LIGO Project (2007), URL <http://www.ligo.caltech.edu/docs/M/M060056-08/M060056-08.pdf>.
 - [3] F. Acernese et al., Classical and Quantum Gravity **23**, S635 (2006).
 - [4] L. Blanchet and B. Sathyaprakash, Phys.Rev.Lett. **74**, 1067 (1995).
 - [5] C. M. Will, Living Reviews in Relativity **9** (2006), URL <http://www.livingreviews.org/lrr-2006-3>.
 - [6] B. S. Sathyaprakash and B. F. Schutz, Living Rev. Rel. **12**, 2 (2009), arXiv:0903.0338.
 - [7] C. K. Mishra, K. G. Arun, B. R. Iyer, and B. S. Sathyaprakash (2010), 1005.0304.
 - [8] N. Yunes and F. Pretorius, Phys. Rev. D **80**, 122003 (2009), 0909.3328.
 - [9] R. Kerr, Phys. Rev. Lett. **11**, 237 (1963).
 - [10] C. Vishveshwara, Nature **227**, 936 (1970).
 - [11] E. Berti, V. Cardoso, and A. O. Starinets, Class. Quant. Grav. **26**, 163001 (2009), 0905.2975.
 - [12] R. Ruffini and J. A. Wheeler, Physics Today **24**, 30 (1971).
 - [13] E. W. Leaver, Proc. R. Soc. Lond. **402**, 285 (1985).
 - [14] O. Dreyer, B. Kelly, B. Krishnan, L. S. Finn, D. Garrison, and R. Lopez-Aleman, Class. Quantum Grav. **21**, 787 (2004), gr-qc/0309007.
 - [15] V. Berti, E. Cardoso and C. Will, Phys. Rev. D **6**, 064030 (2006).
 - [16] E. Berti, J. Cardoso, V. Cardoso, and M. Cavaglià, Phys. Rev. **D76**, 104044 (2007), gr-qc/0501068.
 - [17] I. Kamaretsos, M. Hannam, S. Husa, and B. Sathyaprakash (2011), gr-qc/1107.0854.
 - [18] M. Punturo, M. Abernathy, F. Acernese, B. Allen, N. Andersson, et al., Class.Quant.Grav. **27**, 194002 (2010).
 - [19] B. Sathyaprakash, M. Abernathy, F. Acernese, P.-S. N. Andersson, K. Arun, et al. (2011), to appear in *Proceedings of the Rencontres de Moriond Meeting, March 20-27, La Thuille, Italy*, gr-qc/1108.1423.
 - [20] T. Li, W. Del Pozzo, S. Vitale, C. Van Den Broeck, M. Agathos, et al. (2011), 1110.0530.
 - [21] J. Veitch and A. Vecchio, Phys. Rev. D **81**, 062003 (2010).
 - [22] LSC Algorithm Library software, see URL: <http://www.lsc-group.phys.uwm.edu/lal>.
 - [23] O. Jennrich, A. Petiteau, and E. Porter, Tech. Rep., The ELISA(NGO) Science Performance Task Force (2011), URL https://lisa-light.aei.mpg.de/lisa-light/pub/DetectorConfigurations/FinalConfiguration/ELISA-NGO_FinalConfig.pdf.

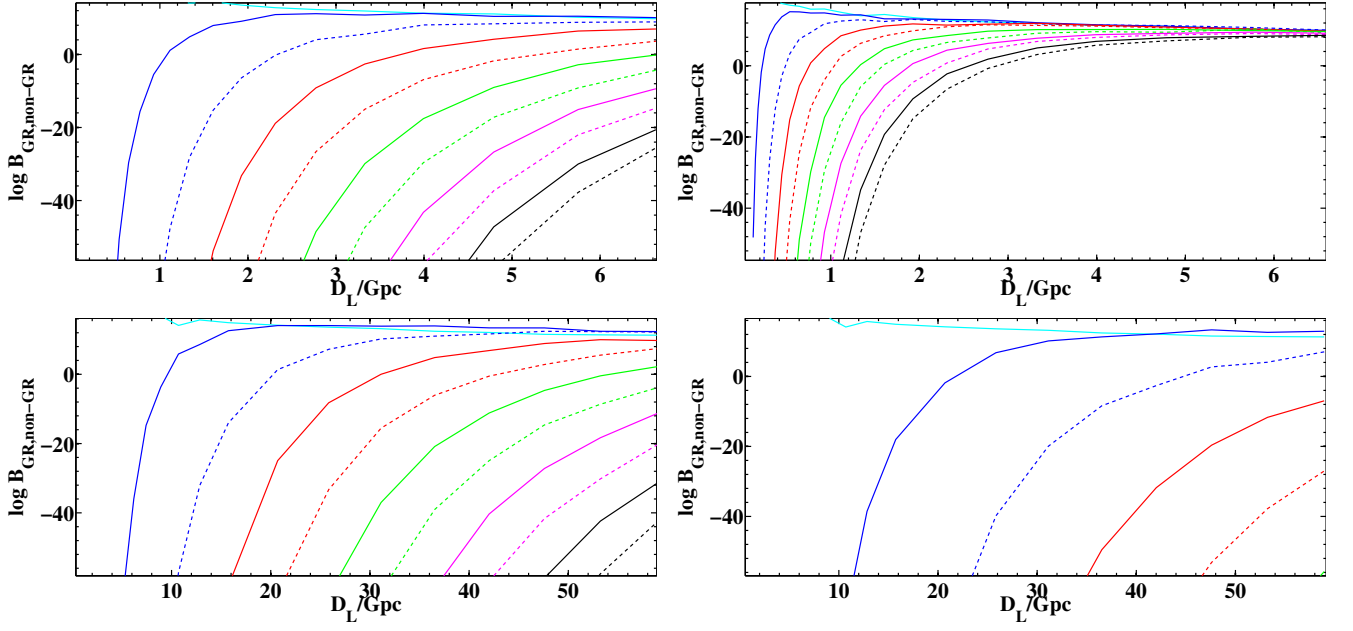


FIG. 5: The differences in evidence for the GR and non-GR models is plotted against the luminosity distance to the source, for observation of ringdown signals from a $500M_{\odot}$ black hole in ET (top panels) and $10^8 M_{\odot}$ black hole in NGO (bottom panels). The non-GR model is simulated by varying either $\Delta\hat{\omega}_{22}$ (left panels) or $\Delta\hat{\tau}_{22}$ (right panels) as compared to their GR values of 0. $\Delta\hat{\omega}_{22}$ and $\Delta\hat{\tau}_{22}$ are varied over the range 0 to -0.1 in steps of -0.01 in the case of ET and over the range 0 to -0.01 in steps of -0.001 in the case of NGO, while keeping all other parameters as for GR. The different curves in each panel correspond to different values of the non-GR parameter, starting with 0 for the top most curve and changing by either -0.01 (top panels) or -0.001 (bottom panels). An evidence of -10 or smaller is considered good enough to discriminate a non-GR model from GR model.

[24] E. Wright, The Publications of the Astronomical Society of the Pacific **118**, 510102 (2006).